

NuSTAR OBSERVATIONS OF X-RAY BURSTS FROM THE MAGNETAR 1E 1048.1–5937

HONGJUN AN¹, VICTORIA M. KASPI^{1,10}, ANDREI M. BELOBORODOV², CHRYSYA KOUVELIOTOU³, ROBERT F. ARCHIBALD¹,
STEVEN E. BOGGS⁴, FINN E. CHRISTENSEN⁵, WILLIAM W. CRAIG^{4,6}, ERIC V. GOTTHELF², BRIAN W. GREFFENSTETTE⁷,
CHARLES J. HAILEY², FIONA A. HARRISON⁷, KRISTIN K. MADSEN⁷, KAYA MORI², DANIEL STERN⁸, AND WILLIAM W. ZHANG⁹

¹ Department of Physics, McGill University, Montreal, Quebec, H3A 2T8, Canada

² Columbia Astrophysics Laboratory, Columbia University, New York, NY 10027, USA

³ Space Science Office, ZP12, NASA Marshall Space Flight Center, Huntsville, AL 35812, USA

⁴ Space Sciences Laboratory, University of California, Berkeley, CA 94720, USA

⁵ DTU Space, National Space Institute, Technical University of Denmark, Elektrovej 327, DK-2800 Lyngby, Denmark

⁶ Lawrence Livermore National Laboratory, Livermore, CA 94550, USA

⁷ Cahill Center for Astronomy and Astrophysics, California Institute of Technology, Pasadena, CA 91125, USA

⁸ Jet Propulsion Laboratory, California Institute of Technology, Pasadena, CA 91109, USA

⁹ Goddard Space Flight Center, Greenbelt, MD 20771, USA

Received 2014 March 6; accepted 2014 June 12; published 2014 July 3

ABSTRACT

We report the detection of eight bright X-ray bursts from the 6.5 s magnetar 1E 1048.1–5937, during a 2013 July observation campaign with *the Nuclear Spectroscopic Telescope Array*. We study the morphological and spectral properties of these bursts and their evolution with time. The bursts resulted in count rate increases by orders of magnitude, sometimes limited by the detector dead time, and showed blackbody spectra with $kT \sim 6\text{--}8$ keV in the T_{90} duration of 1–4 s, similar to earlier bursts detected from the source. We find that the spectra during the tail of the bursts can be modeled with an absorbed blackbody with temperature decreasing with flux. The burst flux decays followed a power law of index 0.8–0.9. In the burst tail spectra, we detect a ~ 13 keV emission feature, similar to those reported in previous bursts from this source as well as from other magnetars observed with the *Rossi X-ray Timing Explorer*. We explore possible origins of the spectral feature such as proton cyclotron emission, which implies a magnetic field strength of $B \sim 2 \times 10^{15}$ G in the emission region. However, the consistency of the energy of the feature in different objects requires further explanation.

Key words: pulsars: individual (1E 1048.1–5937) – stars: magnetars – stars: neutron – X-rays: bursts

Online-only material: color figures

1. INTRODUCTION

Magnetars are isolated neutron stars that have very high magnetic-field strengths inferred from the high spin down rate, typically greater than 10^{14} G (e.g., Vasisht & Gotthelf 1997; Kouveliotou et al. 1998; Olausen & Kaspi 2014, for a catalog of magnetars). Their X-ray luminosities are often greater than their spin-down power, and theorized, therefore, to be powered by the decay of intense internal magnetic fields (Duncan & Thompson 1992; Thompson & Duncan 1995, 1996). The decay of the magnetic field may gradually build up stress in the crust, which can fracture it and/or twist the external magnetic field, causing short X-ray and soft-gamma-ray bursts (Feroci et al. 2001; Lenters et al. 2003; Göğüş et al. 2011) and sudden flux increases (Thompson et al. 2002; Beloborodov 2009). Historically, two classes of X-ray pulsars were thought to be magnetars: anomalous X-ray pulsars (AXPs) whose X-ray luminosities exceed the spin-down power, and soft gamma repeaters (SGRs) which show repeated soft gamma-ray bursts. However, distinction between the two classes has been significantly blurred (Gavriil et al. 2002; Kaspi et al. 2003). There are 26 magnetars discovered to date with various spectral and temporal properties (see Olausen & Kaspi 2014).¹¹

Magnetar bursts have a variety of morphologies, including short (~ 100 ms) symmetric bursts, multiple peaked bursts, those with fast rises and longer decays, and some which exhibit very

long extended “tails” (see, e.g., Woods et al. 2005; Gavriil et al. 2006). Previous studies have suggested relationships between burst intensity and tail energetics (Lenters et al. 2003; Woods et al. 2005) and even the possibility of two distinct types of bursts (Woods et al. 2005). Burst spectra are generally described with thermal models (van der Horst et al. 2012) although there has been evidence for spectral features in some bursts (Gavriil et al. 2002, 2011; Woods et al. 2005; Dib et al. 2009).

The magnetar 1E 1048.1–5937 is relatively active, often showing X-ray bursts and unstable timing behavior. Its spin period is 6.46 s, and the spin inferred surface magnetic-field strength is $B = 4 \times 10^{14}$ G. In quiescence, it shows a spectrum which is well described with a blackbody plus power-law model having $kT \sim 0.6$ keV and $\Gamma \sim 2.9$ (Tam et al. 2008). The distance to the source is estimated to be 9 kpc (Durant & van Kerkwijk 2006), which we use throughout this paper. Interestingly, it is the first AXP in which X-ray bursts were seen (Gavriil et al. 2002), and has shown several more bursts since then (Dib et al. 2009), hereby blurring the distinction between the AXP and SGR classes (see also Kaspi et al. 2003, for 1E 2259+586). Another interesting property of 1E 1048.1–5937’s bursts is a possible emission feature at ~ 13 keV in the spectrum which was previously seen during its 2002 burst in *Rossi X-ray Timing Explorer* (*RXTE*) data (Gavriil et al. 2002; Dib et al. 2009). Similar spectral features have been seen in X-ray bursts from other magnetars as well, all with *RXTE* (XTE J1810–197, 4U 0142+61; Woods et al. 2005; Gavriil et al. 2011).

In this paper, we report on the spectral and temporal properties of eight new bursts from 1E 1048.1–5937 detected

¹⁰ Lorne Trottier Chair; Canada Research Chair.

¹¹ See the online magnetar catalog for a compilation of known magnetar properties: <http://www.physics.mcgill.ca/~pulsar/magnetar/main.html>.

serendipitously with the *Nuclear Spectroscopic Telescope Array* (*NuSTAR*) in 2013 July. We describe the observations and data reduction in Section 2, and show the data analysis and results in Section 3. We then discuss the implications of the analysis results (Section 4) and conclude in Section 5.

2. OBSERVATIONS

NuSTAR operates in the 3–79 keV band, and is the most sensitive satellite in the ~ 10 –79 keV band thanks to its unique focusing capability in this energy range. The energy resolution is 400 eV at 10 keV (FWHM), and the temporal resolution is $2 \mu\text{s}$ (see Harrison et al. 2013 for more details). Its excellent temporal and spectral resolutions together with the high sensitivity above ~ 10 keV are optimal for the study of burst properties of magnetars because such events are very brief ($\sim \text{ms}$) and sometimes spectrally very hard.

1E 1048.1–5937 was observed with *NuSTAR* on 2013 July 17–27 with a total net exposure of ~ 320 ks (Obs. ID 30001024001–7). A 70 ks joint *XMM-Newton* observation (Obs. ID: 0723330101) was conducted using the small window mode for MOS1/2 and the full frame mode for PN on 2013 July 22 to extend the spectral coverage down to ~ 0.5 keV where the thermal component is dominant. The source was not known to be in a particularly active state at the time of the observation. During the *NuSTAR* observations, eight X-ray bursts from the source were detected to our surprise, with one simultaneous detection in the *XMM-Newton* data.

The *NuSTAR* data were processed with nupipeline 1.3.1 along with CALDB version 20131007 using standard filters except for PSDCAL. We set PSDCAL=NO in order to recover more exposure by slightly sacrificing the pointing accuracy.¹² We verified that the exposure increases and that the imaging, timing, and spectral analysis results are consistent with those obtained with PSDCAL=YES. The *XMM-Newton* data were processed with Science Analysis System 12.0.1 using the standard filtering process. We then further processed the event files for analysis as described below.

3. DATA ANALYSIS AND RESULTS

3.1. Burst Morphology

In order to search for bursts, we extracted events in an aperture of $60''$ around the source position in the *NuSTAR* image, and produced barycenter-corrected light curves with a bin size of 0.5 s. We then searched for time bins having a significantly larger number of counts compared with the persistent level which was extracted from the source region (and which is dominated by the persistent flux from the source) in 10 pulse periods (~ 64 s) prior to the time bin that is being searched. The average count rate of the persistent emission was 0.2 count s^{-1} in the 3–79 keV band within the $R = 60''$ aperture (see Figure 1). We further verified that the count rate in the off-source region did not show any significant increase (e.g., due to a background flare) over any short time interval. We then calculated the Poisson probability of the observed count given the background rate for each time bin. To be considered significant, we required a $>3\sigma$ chance probability p after considering the number of trials. In total, we detected eight bursts with high significance, each one having $p < 10^{-10}$. We also tried different bin sizes (e.g., 0.01–100 s), and found similar results, although the significance changes

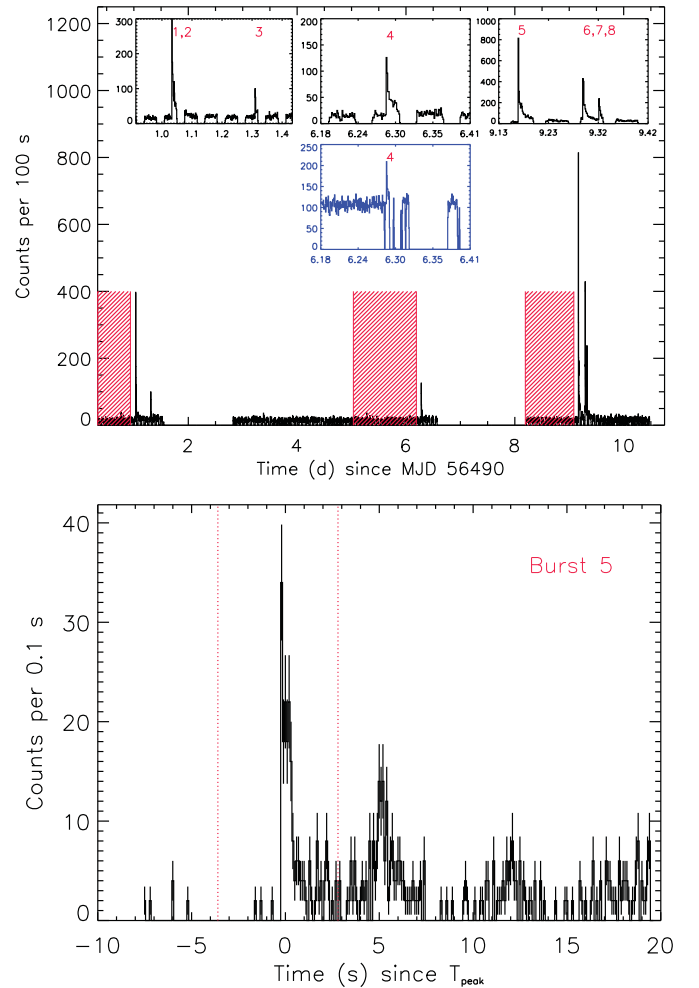


Figure 1. Top: 3–79 keV light curve for the *NuSTAR* observations with Modules A and B combined. Time intervals for pre-burst background extraction are shown in red hatched lines (see Sections 3.3 and 3.4). Insets show zoomed-in 3–79 keV *NuSTAR* and 0.5–10 keV *XMM-Newton* light curves (blue) around the bursts with burst numbers. Bottom: a 30 s light curve around burst 5 in the 3–79 keV band. $T = 0$ is set to the burst peak time, and red vertical lines show one pulse period in which we characterize the burst morphology (see Equation (1) and Table 1).

(A color version of this figure is available in the online journal.)

depending on the binning, and some bursts are not significantly detected on some timescales. The bursts 2 and 7 are not detected on a long timescale (100 s), and we do not report their tail properties.

We note that many time bins immediately after a burst were detected significantly above quiescence. The significantly detected time bins are likely those of the burst tail emission or the peaks of the source pulsations which are visible immediately after the burst (e.g., see Figure 1 bottom). However, there may be time bins with significantly higher count rates which are produced by an independent burst event. To investigate whether these significantly detected bins after a burst were independent events and not related to the burst tail or the pulse peaks, we proceeded as follows. We extracted a ~ 50 s light curve after a burst and characterized it with a decay model, specifically an exponentially decaying sine plus an exponential decay plus a constant. We then searched for time bins ($\Delta T = 0.05$ –1 s) having counts above the decay model with $\gtrsim 3\sigma$ confidence, and found none. Therefore, we conclude that there were only eight significant bursts during the observation. The *NuSTAR*

¹² http://heasarc.gsfc.nasa.gov/docs/nustar/analysis/nustar_swguide.pdf

Table 1
Summary of *NuSTAR*-detected Bursts

Burst	T_0^a (day)	ϕ^b	T_r^a (s)	T_f^a (s)	A^a (counts s $^{-1}$)	C_1 (cps)	C_2^a (cps)	T_{90}^c (s)	kT^d (keV)	L_{90}^d (10 37 erg s $^{-1}$)
1	1.0330396	0.477 $^{+0.006}_{-0.009}$	1.7 $^{+0.2}_{-0.2}$	0.07 $^{+0.19}_{-0.05}$	56 $^{+6}_{-6}$	1.8 $^{+0.7}_{-0.6}$	8 $^{+2}_{-2}$	4.0 $^{+0.5}_{-0.5}$	6.3(8)	1.6(4)
2	1.0405240	0.555 $^{+0.001}_{-0.001}$	0.012 $^{+0.010}_{-0.007}$	0.03 $^{+0.01}_{-0.01}$	170 $^{+70}_{-60}$	2.7 $^{+0.8}_{-0.7}$	3 $^{+2}_{-1}$	0.10 $^{+0.03}_{-0.03}$
3	1.3100872	0.9177 $^{+0.001}_{-0.0006}$	0.06 $^{+0.02}_{-0.02}$	<0.018	190 $^{+60}_{-50}$	1.6 $^{+0.5}_{-0.4}$	4 $^{+1}_{-1}$	0.17
4	6.2812256	0.6631 $^{+0.0012}_{-0.0006}$	0.10 $^{+0.02}_{-0.02}$	<0.019	170 $^{+50}_{-40}$	0.7 $^{+0.3}_{-0.2}$	5 $^{+2}_{-1}$	0.26
5	9.1684044	0.5052 $^{+0.0002}_{-0.0005}$	<0.007	0.42 $^{+0.04}_{-0.03}$	360 $^{+30}_{-30}$	3 $^{+2}_{-1}$	17 $^{+4}_{-3}$	0.98	8.0(8)	16(3)
6	9.2942137	0.7269 $^{+0.0034}_{-0.0002}$	0.8 $^{+0.1}_{-0.1}$	<0.055	100 $^{+10}_{-10}$	8 $^{+2}_{-2}$	16 $^{+4}_{-4}$	2.0	7(1)	4(1)
7	9.2973844	0.155 $^{+0.005}_{-0.002}$	<0.03	0.17 $^{+0.05}_{-0.04}$	110 $^{+30}_{-30}$	3 $^{+1}_{-1}$	7 $^{+1}_{-1}$	0.46
8	9.3254520	0.4116 $^{+0.0001}_{-0.0001}$	<0.015	0.65 $^{+0.06}_{-0.05}$	170 $^{+20}_{-20}$	1.5 $^{+0.8}_{-0.6}$	4 $^{+2}_{-2}$	1.52	8(1)	5(1)

Notes. Uncertainties are at the 1σ confidence level, and upper limits are at the 90% confidence level.

^a Parameters for the short timescale light curve as defined in Equation (1). T_0 is days since MJD 56490 (TDB).

^b Spin phase corresponding to T_0 , where phase zero is defined at the pulse minimum (56490.3343345727 MJD), same as that for the timing analysis in Figures 2–4.

^c Time interval which includes 90% of the burst counts (the exponential functions in Equation (1)). T_{90} 's for the rising and the falling function were calculated separately and then summed to obtain that for the burst. When only an upper limit is available for T_r or T_f , we used the upper limit to calculate T_{90} and show it without uncertainties.

^d Spectral parameters for a blackbody spectrum corresponding to T_{90} : blackbody temperature kT and bolometric luminosity L_{90} .

light curve is shown in Figure 1, and the burst properties are listed in Table 1. The burst light curves all exhibit rises and decays of a few seconds with relatively long tails (\sim ks).

After we identified the bursts, we extracted events in a one period interval that contains the burst in order to further characterize the temporal properties of the bursts on very short timescales. Note that we included one more period for the bursts that occurred late in pulse phase so as not to miss the falling tail. We fit the time series to an exponentially rising and falling function

$$F(t) = \begin{cases} Ae^{(t-T_0)/T_r} + C_1 & t < T_0, \\ (A - C_2)e^{-(t-T_0)/T_f} + C_1 + C_2 & t \geq T_0, \end{cases} \quad (1)$$

where A is the amplitude, T_0 is the burst peak time, T_r is the rising time, T_f is the falling time, and $C_{1,2}$ are constants. We note that the decay of a burst has typically been modeled with a double exponential function (e.g., Gavriil et al. 2011), but here we replace the second exponential with a constant (C_2) because this suffices for describing our data in the chosen time span, which is much smaller than the decay constant of any second exponential. Since the timescales are very short, and there are only a few events in each \sim ms time bin, we used maximum-likelihood optimization. Furthermore, we used events in the whole detector because having a well sampled time series is important in the fitting. We modeled the background with another constant, C_1 . The results of the fitting are presented in Table 1.

We note that the observed count rate is smaller than the incident rate for the brightest burst due to detector deadtime (Harrison et al. 2013). Since the maximum count rate for burst 4 is comparable to the maximum count rate that the *NuSTAR* detectors can process (\sim 400 counts s $^{-1}$ per module), we consider the effect of deadtime in order to calculate the incident count rate, R_i , via the following relation:

$$R_i = \frac{R_o}{1 - R_o \tau_D}.$$

Here R_o is the observed count rate, and τ_D is the detector dead time (\sim 2.5 ms) for each observed event. The incident peak count

rates are higher, and the rising and the falling times are smaller than the observed values in Table 1, but within a factor of \sim 2 of the true values. For example, the maximum observed count rate for burst 4 is \sim 200 counts s $^{-1}$ per module, and the incident rate is estimated to be \sim 400 counts s $^{-1}$ per module for this burst.

3.2. Timing Analysis

In order to measure the pulse period, we extracted events within radii of $60''$ and $32''$ for *NuSTAR* and *XMM-Newton*, respectively, and applied a barycenter correction to the events. We then subdivided the total observations into 51 and 48 sub-intervals so that each sub-interval has \sim 1200 and \sim 2400 events to have at least \sim 20 counts in a phase bin ($\Delta\phi = 1/32$) for *NuSTAR* (3–79 keV) and *XMM-Newton* (0.5–10 keV), respectively. The typical duration of each sub-interval is \sim 15 ks and \sim 1 ks for *NuSTAR* and *XMM-Newton*, respectively, but varies depending on the source luminosity. We then fit the pulse profile to a Gaussian plus constant function to measure the phase of each profile. The Gaussian plus constant function describes the pulse profiles well, and we show the measured phases in Figure 2 and examples of pulse profiles in Figures 3 and 4. We note that cross-correlating the pulse profiles gives similar results. The phases are fitted to a linear function $\phi(t) = \phi_0 + ft$, where ϕ_0 is the reference phase, and f is the frequency. We did not include the frequency derivative because it is not required. In fitting, we ignored \sim 10–90 ks of data after the bursts because, interestingly, there is a relatively large phase shift immediately post-burst which contaminates the result (see Figure 2). From the analysis, we found the period to be 6.46168155(6) s, but were not able to constrain the period derivative well.

In order to see if the large phase shift during the bursts (see Figure 2) is related to the rotation of the star, we measured the shift in different energy bands (*NuSTAR* and *XMM-Newton*) and found that it is much smaller in the soft band than in the hard band (e.g., see $T \sim$ 6 days in Figure 2). We also verified that the energy dependence of the post-burst phase shifts is observed in the *NuSTAR* and the *XMM-Newton* data individually, and the large phase shift at \sim 6 days in the *NuSTAR* data was seen in the *XMM-Newton* hard-band data (4–10 keV) as well. These imply

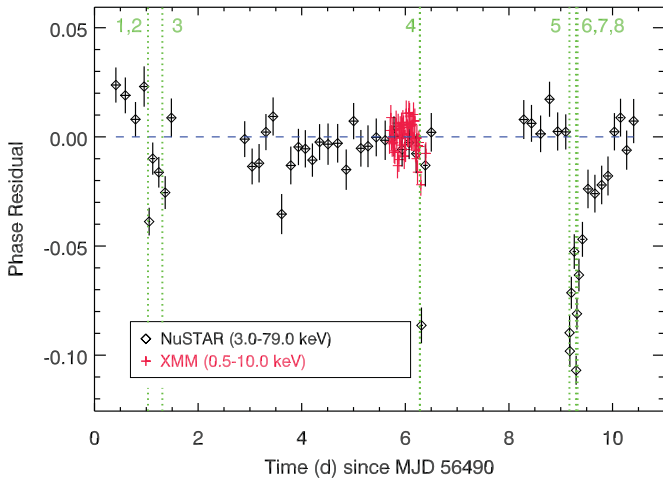


Figure 2. Measured timing residuals for $P = 6.46168155$ s for the *NuSTAR* data in the 3–79 keV band (black) and the *XMM-Newton* data in the 0.5–10 keV band (red). The best-fit function is shown in a blue horizontal dashed line and the burst times are shown in green vertical dotted lines.

(A color version of this figure is available in the online journal.)

that the phase shift is not due to the rotation of the source; if it were, we would expect the shift to be independent of energy.

Figures 3 and 4 present pre- and post-burst pulse profiles for 1E 1048.1–5937 from *NuSTAR* and *XMM* data, respectively. The pre- and post-burst pulse profiles are qualitatively similar except for the phase shifts discussed above. Some “spiky” features appeared in some post-burst profiles (e.g., Figure 3), which are likely to be statistical fluctuations. However, we note that another hard peak at phase ~ 0.3 in the 3–10 keV band seemed to appear in the *XMM-Newton* pulse profile immediately post-burst (see Figure 4(b)).

3.3. Burst Spectroscopy

Next, we focus on the spectra of the bursts and their tails. The spectrum of the full data will be presented elsewhere (R. F. Archibald 2014, in preparation). In order to characterize a burst spectrum, we calculated the T_{90} for each event; these are shown in Table 1. We note that deadtime is likely to have affected the burst light curves (Section 3.1) since we used unbinned events and did not correct for the deadtime for individual events. A spectrum, integrated over a time interval, is less affected since the deadtime effect is corrected for every 1 s time bin, which is precise enough unless the spectral shape rapidly changes within the 1 s time bin. We assume that the spectral shape (i.e., kT) of the source did not change significantly in one second, and hence that the deadtime effect is properly corrected.

We extracted source events in a circle with radius $60''$ in the time interval T_{90} for each burst. Backgrounds were extracted from the pre-burst time intervals shown in Figure 1 (red hatched regions). The pre-burst spectra include photons up to ~ 15 keV above the background and are well described with a power law plus blackbody or two blackbody models, both having 3–79 keV flux of 4×10^{-12} erg s $^{-1}$ cm $^{-2}$. The luminosity for the assumed two blackbody model is 1×10^{35} erg s $^{-1}$ (see R. F. Archibald 2014, in preparation for more detail). Note that the extraction times are very short, so background contamination is very small (~ 0.2 cps including the persistent source emission).

We fit the spectrum to an absorbed blackbody and an absorbed power law using the C statistic (`cstat` in XSPEC 12.8.1) in the 3– E_{\max} keV band, where E_{\max} was between 30 and 50 keV depending on the source flux. We verified that the fit results did not change over a broad range of the upper energy limit. There were not many events in each spectrum, and we found that both spectral models provided good fits. Since *NuSTAR* is not sensitive in the energy band below 3 keV, we were not able to

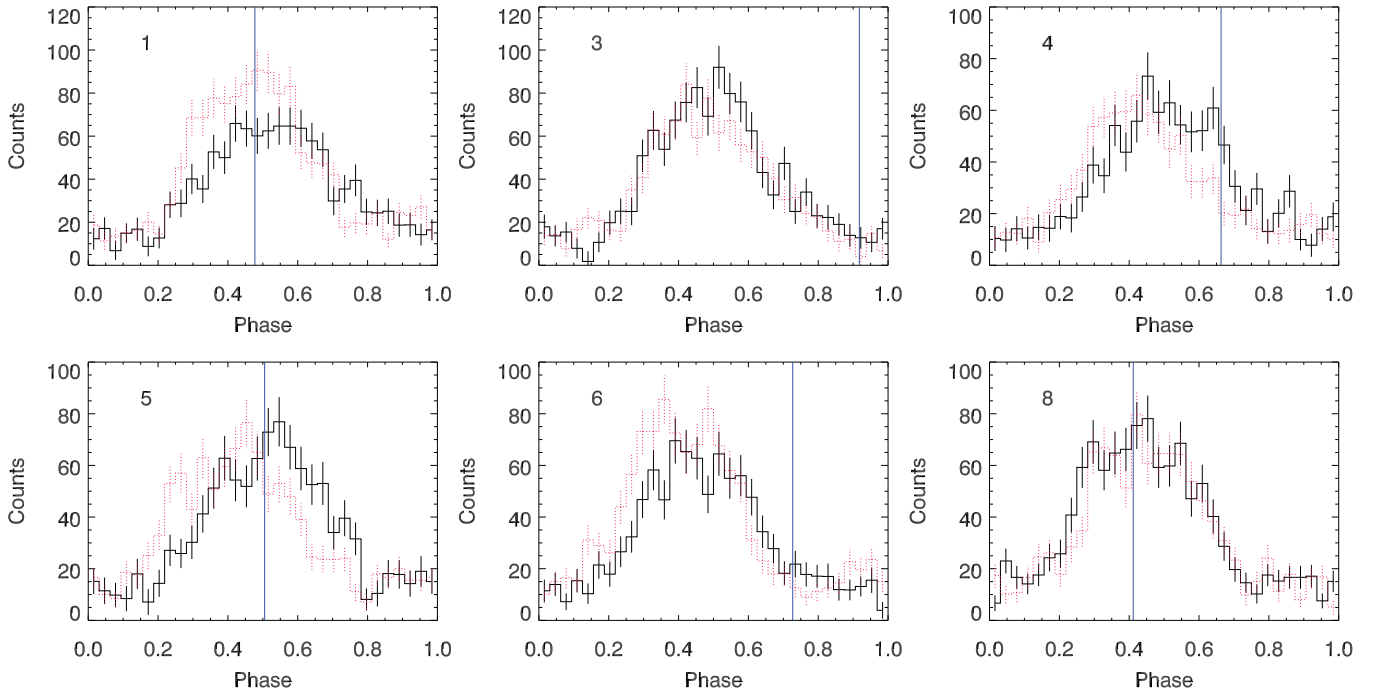


Figure 3. Immediate pre- (black) and post-burst (red) *NuSTAR* pulse profiles for bursts 1, 3, 4, 5, 6, and 8 in the 3–79 keV band. T_{90} burst intervals were not included in making these profiles. Backgrounds were subtracted, and the integration times were chosen so that each pulse profile had ~ 1200 counts. Burst numbers are shown in the plots for reference. Vertical lines in the plots are the phases corresponding to the T_{90} in Equation (1) for each burst. Note that the pre-burst profiles of burst 5 and 6 include significant tail emission of burst 4 and 5, respectively.

(A color version of this figure is available in the online journal.)

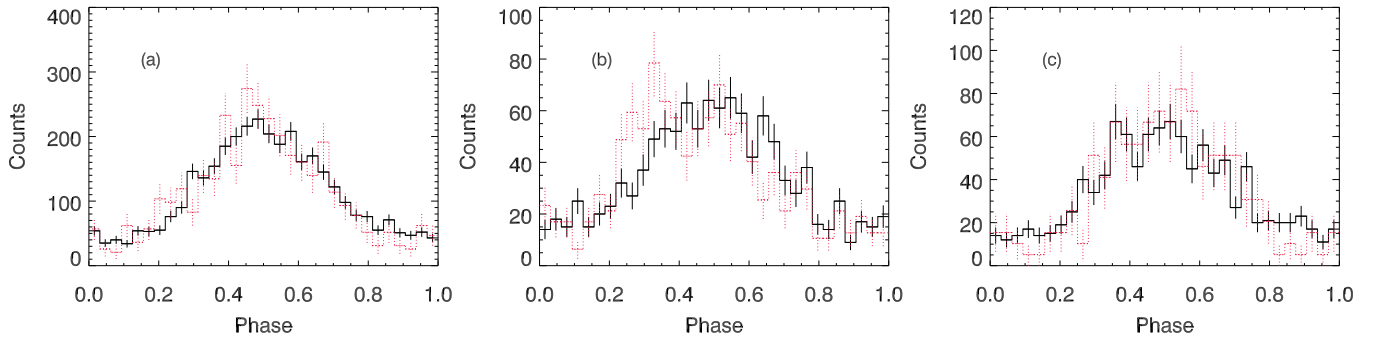


Figure 4. *XMM-Newton* pulse profiles of pre- and post-burst time intervals of burst 4 in the 0.5–3 keV (black) and 3–10 keV (red) bands for the pre-burst (a), immediately post-burst in a time interval of 2–2000 s after the burst peak time measured with *NuSTAR* (b), and late post-burst (c) time intervals. Backgrounds were subtracted, and the integration times were 2 ks. The hard-band profiles were normalized to the soft-band ones for each plot.

(A color version of this figure is available in the online journal.)

measure N_{H} , and so we froze it at the value measured previously ($0.97 \times 10^{22} \text{ cm}^{-2}$; Tam et al. 2008).

We show the best-fit parameters for the blackbody model in Table 1. Note that the numbers of events in T_{90} for the bursts 2, 3, 4, and 7 were smaller than ~ 10 , and the spectral parameters were not reasonably constrained. We also tried to fit the data using the usual χ^2 method with Churazov weighting (Churazov et al. 1996) after grouping the spectra to have at least 5 counts per bin found that the results are consistent with those obtained using the C statistic.

Although single component models provide good fits, we also tried to fit the spectra to double blackbody models, since magnetars sometimes show double blackbody spectra during bursts (e.g., Lin et al. 2012). The second blackbody component is not statistically required for any bursts in our data. However, it is possible that there was an undetected high-temperature blackbody component as was seen by, e.g., Lin et al. (2012). Therefore, we measure a luminosity upper limit for a high-temperature blackbody component. We first froze the parameters of the single blackbody fit at the values obtained above, added another high-temperature blackbody, and scanned the parameter space of the high-temperature blackbody using the `steppar` command in XSPEC. The luminosity upper limit increased with kT as expected since *NuSTAR* becomes less sensitive as kT goes up. We measured the 90% luminosity upper limit to be $0.2\text{--}8 \times 10^{38} \text{ erg s}^{-1}$ for $kT = 15 \text{ keV}$, for example.

We also set an upper limit on flux of a possible lower temperature blackbody, similar to that seen in the bursts of SGR 1900+14 (Israel et al. 2008), where the authors found a low-temperature blackbody component with kT as low as $\sim 2 \text{ keV}$ having comparable luminosity with the high temperature component. We followed the same procedure that we did above for the high-temperature component but with $kT = 2 \text{ keV}$, and found that the luminosity upper limits are $2\text{--}10 \times 10^{36} \text{ erg s}^{-1}$, always an order of magnitude smaller than the burst luminosities in Table 1.

3.4. Tail Spectroscopy

We also characterized the post-burst tail emission for the bursts with a significant tail (bursts 1, 3, 4, 5, 6, and 8). In order to minimize the effect of the burst, we removed the T_{90} intervals in this analysis. We extracted events from a circular region of a radius $60''$ centered on the source, and the background from a source-free region on the same detector in a radius $90''$ in the *NuSTAR* data. Since the source spectrum may change significantly during a burst, we subdivided each burst into

several sub-intervals such that each interval has ~ 200 counts, in order to have good time resolution and to be statistically sensitive to the change in the spectral parameters in time. The integration times were very short at early times after a burst, and we could not collect enough background events. Therefore, for those sub-intervals we used a longer background exposure (1 ks).

We fit the spectrum for each sub-interval to an absorbed blackbody and an absorbed power-law model using the C statistic in XSPEC. The fit ranges were $3\text{--}E_{\text{max}}$, where E_{max} was 20–50 keV. Both blackbody and power-law models are acceptable, although blackbody models provide better fits in general, giving fit statistics smaller by ~ 10 on average (~ 200 dof). We show the results for the blackbody fit in Figures 5(a)–(c). Note that the persistent emission is included in the spectra in this case.

We then tried to characterize the spectral evolution after removing the persistent emission. The persistent level was extracted from the source region but in the pre-burst time intervals shown in Figure 1. The source seemed to return to the persistent level $\sim 2\text{--}3 \text{ ks}$ after a burst, and thus we analyzed only the first $\sim 2 \text{ ks}$ after a burst.

We find that the spectral parameters and their evolution are similar to those of the spectra with the persistent emission. This is expected because the burst tails dominate over the persistent emission during the time intervals.

The bursts have very long tails ($\sim \text{ks}$) as is often seen in magnetar bursts (e.g., Gavriil et al. 2011). We have measured the timescales of the decaying tails by fitting the light curve. However, as we show above (Figure 5), the spectrum evolves significantly over a relatively short timescale, and hence the measured light curves obtained using energy-integrated count rates will be different for different telescopes because of differences in the energy responses. In order to estimate the decay timescales in an instrument-independent way, we directly measure the spectral evolution of the bursts. We fit the time evolution of the spectral parameters for the tail spectra including the persistent emission with a power-law decay,

$$S = S_0 t^{-\alpha} + S_1, \quad (2)$$

where S is the spectral parameter, S_0 is the value of the parameter at $t = 1 \text{ s}$, α is the decay index, and S_1 is a positive constant corresponding to the persistent emission. We show the results in Table 2. Note that we do not show the results for burst 3 because we were not able to constrain its decay with the given data.

We note that there might be some less significant bursts in the tails. For example, bursts 2 and 7 occurred at $\sim 600 \text{ s}$ and $\sim 200 \text{ s}$

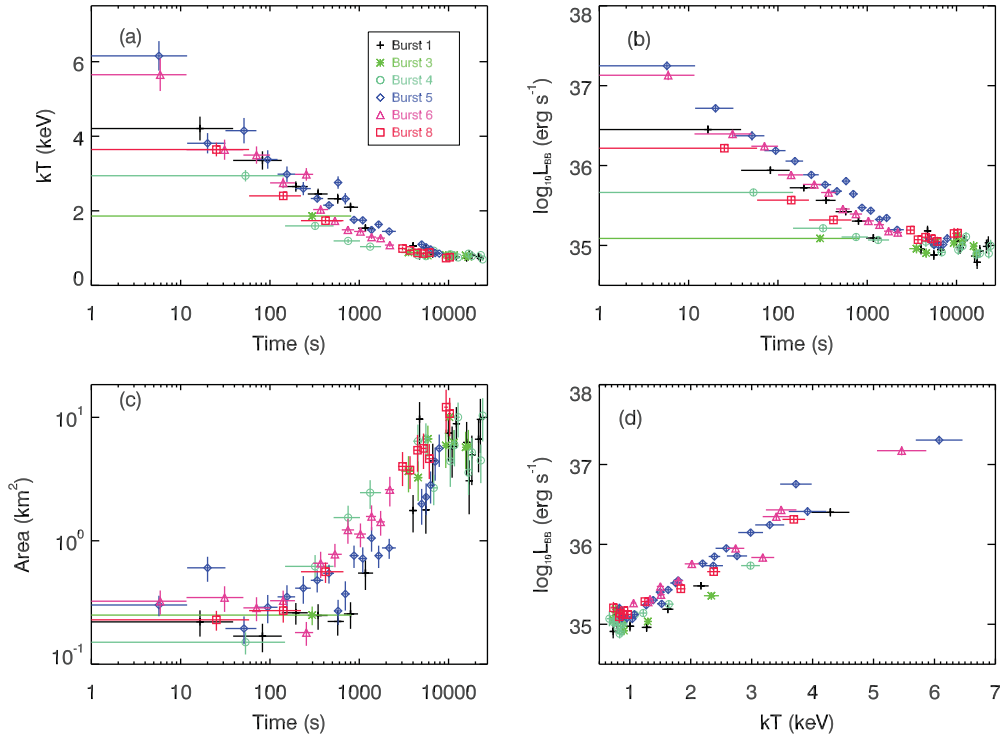


Figure 5. Time evolutions of the spectral parameters of the blackbody model for the persistent plus tail spectra and kT vs. L_{BB} for tail spectra of the six bursts (bursts 1, 3, 4, 5, 6, and 8). (a) Blackbody temperature, kT , (b) bolometric luminosity, L_{BB} , (c) blackbody area, and (d) kT vs. L_{BB} .

(A color version of this figure is available in the online journal.)

Table 2
Parameters for the Spectral Evolution of the Tails

Burst	S_0 (10^{35} erg s^{-1})	α_L	α_{kT}	S_1 (10^{35} erg s^{-1})
1	290(60)	0.81(4)	0.28(1)	0.69(7)
4	90(50)	0.8(1)	0.57(5)	0.84(6)
5	640(90)	0.82(3)	0.27(1)	0.5(1)
6	560(120)	0.87(5)	0.29(1)	0.7(2)
8	420(150)	1.03(9)	0.28(4)	1.21(8)

Note. Uncertainties are at the 1σ confidence level.

into the tail of burst 1 and 6, respectively. Also, there seems to be an increase in kT and L_{BB} at ~ 600 s after burst 5 although we did not find any significant burst. Undetected or less significant bursts may bias α to a smaller value. Also note that we assumed that the luminosity at late times can freely vary in the fit, and the best-fit values for S_1 are $0.5\text{--}1.2 \times 10^{35}$ erg s^{-1} , sometimes smaller than the pre-burst source luminosity. If we freeze S_1 at the pre-burst value of 1×10^{35} erg s^{-1} , α becomes $0.9\text{--}1.0$.

We also analyzed the *XMM-Newton* data to characterize precisely the soft-band (0.5–10 keV) spectrum of the burst 4 tail which is the only burst detected simultaneously with *XMM-Newton* and *NuSTAR*. We extracted source and background events in circles with radius $32''$ for an exposure of ~ 400 s excluding the T_{90} interval, where the background region was $\sim 200''$ north of the source. The *XMM-Newton* count rates were 1.2/1.3 and 4.5 cps for MOS1/2 and PN, respectively. Such count rates will result in spectral distortion of $\lesssim 1\%$ and $\sim 2.5\%$ for MOS1/2 and PN, much smaller than the statistical uncertainties we obtain below. Hence, we used all the MOS1/2 and PN data. We grouped the spectrum to have at least 20 events per spectral bin. We then extracted *NuSTAR* events for the same

time interval, and binned the spectrum to have 20 events per bin, and jointly fit the *XMM-Newton* and the *NuSTAR* data, holding N_{H} fixed at 0.97×10^{22} cm^{-2} . Note that the persistent emission was not removed in these spectra.

Single component models were not acceptable with χ^2/dof of 583/102 and 122/102 for a blackbody and a power law, respectively. A double blackbody model was acceptable with $\chi^2/\text{dof} = 127/100$. But a blackbody plus power-law model provided a better fit ($\chi^2/\text{dof} = 98/100$), and adding one more blackbody slightly improved the fit ($\chi^2/\text{dof} = 96/98$) although it was required only with low significance (F -test probability 40%). Nevertheless, the parameters for the soft spectral component ($kT_1 = 0.6 \pm 0.2$ keV and $\Gamma = 2.5 \pm 0.4$) of the power law plus two blackbody model were similar to those of the quiescent spectrum of the source (Tam et al. 2008), and the hard component ($kT_h = 3.2 \pm 0.4$ keV) is similar to that of the spectrum with the persistent emission removed (see below). When we let N_{H} vary, we obtain similar results as the above with $N_{\text{H}} = 1.2(4) \times 10^{22}$ cm^{-2} .

We also tried to characterize the persistent-emission-removed spectrum of the combined data. Here, the persistent level was extracted from the pre-burst time intervals in the source region for both *NuSTAR* and *XMM-Newton*. A blackbody model was able to fit the data well ($kT = 3.0 \pm 0.2$ keV, $\chi^2/\text{dof} = 96/104$) but a power-law model was not as good ($\chi^2/\text{dof} = 128/104$).

3.5. Spectral Feature

We searched for the spectral feature at ~ 13 keV previously observed from this source's burst spectra (Gavriil et al. 2002, 2011; Dib et al. 2009). As the feature was observed in the $\lesssim 2$ s spectra in the past, we checked if a line feature was statistically required in the burst spectra (see Section 3.3) but found that it is

Table 3
Best-fit Spectral Parameters for the Spectrum of the First 150 s after T_0 for Burst 5

Model ^a	N_{H}^{b} (10^{22} cm^{-2})	kT/Γ (keV)	$L_{\text{BB}}/F_{\text{PL}}^{\text{c}}$	E_{G}^{d} (keV)	σ_{G} (keV)	N_{G} (photon $\text{cm}^{-2} \text{ s}^{-1}$)	χ^2/dof
BB	0.97	4.1(2)	30(2)	70/42
BB + Gauss	0.97	3.8(2)	25(2)	13.2(3)	1.3(3)	$2.1(5) \times 10^{-3}$	39/39
PL	0.97	0.83(7)	12(1)	108/42
PL + Gauss	0.97	1.0(1)	0.8(1)	12.7(2)	1.7(3)	$3.4(6) \times 10^{-3}$	44/39

Notes. Uncertainties are at the 1σ confidence level.

^a BB: blackbody, PL: power law, Gauss: Gaussian line profile.

^b Frozen.

^c Bolometric luminosity in units of $10^{35} \text{ erg s}^{-1}$ for the blackbody model, and the absorption corrected 3–79 keV flux in units of $10^{-9} \text{ erg s}^{-1} \text{ cm}^{-2}$ for the power-law model.

^d Subscript G is used for the Gaussian parameters: line energy (E_{G}), line width (σ_{G}), and normalization (N_{G}).

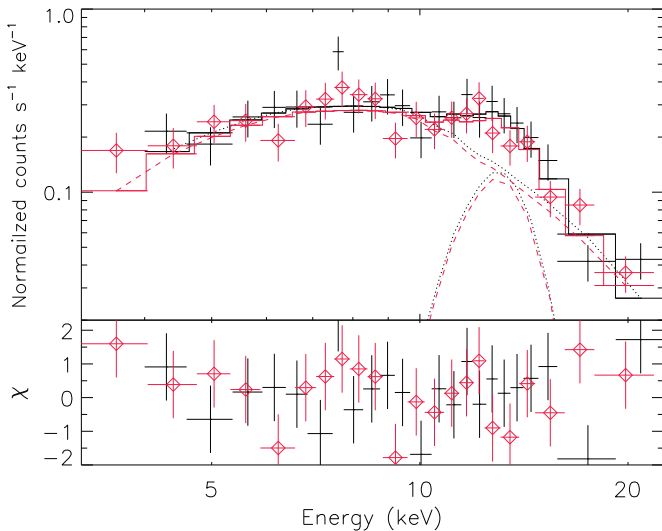


Figure 6. Blackbody plus Gaussian line fit for the 150 s *NuSTAR* spectrum of burst 5.

(A color version of this figure is available in the online journal.)

not. However, as we increased the integration time, we started seeing an enhancement in counts at ~ 13 keV for burst 5.

In order to see if a line feature is statistically required for the bursts and their tail emission, we first extracted a spectrum from the first 150 s of the brightest burst (burst 5). The background was extracted from the pre-burst interval in the source region. We then fit the spectrum in the 3–30 keV band with continuum models (blackbody, power law, and bremsstrahlung), and found that none could describe the data well with χ^2/dof of 70/42 (blackbody), 108/42 (power law), and 147/42 (bremsstrahlung). We also tried combinations of the continuum models, but none improve the fit significantly with χ^2/dof being 67/40, 108/40, 67/40, 67/40 for a double blackbody, a double power-law, a blackbody plus power-law, and a blackbody plus bremsstrahlung models, respectively. In particular, in all these two-component trials, the best-fit parameters of the second component are trivial; the amplitude is not constrained at all, and kT or Γ become ridiculously small or large. However, adding a Gaussian line to a blackbody model provided an acceptable fit ($\chi^2/\text{dof} = 38/40$). We show the spectrum and the blackbody plus Gaussian fit in Figure 6, and the results are presented in Table 3. We repeated the same procedure for spectra in different time intervals (e.g., 100 s, 200 s, and 300 s), and found that the fit improves significantly ($\Delta\chi^2 \gtrsim 20$) by adding a Gaussian line to the blackbody model, from which

we draw the same conclusion as we did with the 150 s spectrum. We conducted the same analysis with the other bursts and found that a blackbody model alone was able to describe their spectra well (for example, $\chi^2/\text{dof} = 39/35$, $p \sim 0.1$ for burst 6).

We used simulations in order to calculate the true significance of the feature in burst 5 and its tail. The spectrum of the source following a burst evolved on a timescale of 150 s. Therefore, we conducted simulations with temporally evolving blackbody spectra. We first divided the 150 s spectrum of burst 5 into five time intervals as shown in Figure 5 and the T_{90} interval, and fit the six spectra to blackbody models after removing the energy range of the feature (11.5–14 keV). We then simulated the six spectra using *fakeit* in XSPEC with the response and background for the actual data, and merged them into one spectrum that represents a 150 s spectrum. For each simulation, we first fit the spectrum to a blackbody, and then calculated the improvement of the fit ($\Delta\chi^2$) by adding a Gaussian line. For the latter fit, we scanned the energy range of the spectrum (4–22 keV) with a step of 1 keV for the initial value of the line energy because the narrow feature can make the fit fall in a local minimum around the initial value. We counted the number of occurrences in which the improvement of the fit in a simulation was larger than that seen in the actual data fit ($\Delta\chi^2 = 31$), and found that this did not occur in 10,000 simulations. The significance of the feature would be even higher if we scan only a smaller energy range (e.g., 11–15 keV) for the Gaussian line energy guided by the previous *RXTE* measurements.

We found that a blackbody model fits the spectra of the feature-removed 150 s data as well as the above simulations. Therefore, we also conducted simulations with a single blackbody continuum model, and found that improvement of fit measured by $\Delta\chi^2$ by adding a Gaussian line model was always smaller than 31 in 10,000 simulations.

We investigated if the feature exists in the spectra without the burst. We removed the T_{90} interval from burst 5 and extracted tail spectra for 100 s, 150 s, 200 s, and 300 s exposures. We then applied the same fitting procedure and found that the same conclusion is valid; for example, single or combinations of continuum models do not fit the 150 s spectrum well with χ^2/dof of 75/39 (blackbody), and 164/39 (power law) while adding a Gaussian line to a blackbody improves the fit significantly, making it acceptable ($\chi^2/\text{dof} = 42/36$). The best-fit Gaussian line parameters are statistically consistent with those we obtained above.

We checked if the spectral feature shifts in energy with phase as seen in the magnetar SGR 0418+5729 (Tiengo et al. 2013). We produced a two-dimensional energy versus phase image as shown in Tiengo et al. (2013), and found no evidence of a shift.

This may be due to the paucity of counts in our case. We also tried to see if the feature is more prominent in some phase intervals than the others, and could not draw any statistically significant conclusion.

4. DISCUSSION

We have reported the first detection of X-ray bursts from magnetar 1E 1048.1–5937 with a focusing hard X-ray telescope. Table 1 summarizes the temporal and spectral properties of the eight bursts detected with *NuSTAR*. The short timescale behaviors of the bursts are different from burst to burst, having T_r and T_f of milliseconds to seconds. All the bursts have relatively long tails (see Figure 5) and their spectra evolve with time. We also found that their peak times are random in phase.

4.1. Temporal Properties of the Bursts and their Tails

Magnetar bursts, including those we have observed for 1E 1048.1–5937, generally exhibit a fast rise and fall, which has been suggested to result from crustal fracture (Thompson et al. 2002) and/or magnetic reconnection (Lyutikov 2003). The pulse phase of the burst peak was previously used to reconstruct the event location and constrain the emission geometry (Woods et al. 2005). Interestingly, the bursts appear to occur at random pulse phases (Table 1), and bursts 2 and 5 may be emitted far from the magnetic axis of the star. Note, however, that the location reconstruction assumes emission beaming along the magnetic field lines, which may not be realistic. A quasi-isotropic burst could be visible from any direction unless it is eclipsed by the neutron star. The probability of eclipse is significantly reduced by gravitational light bending, which makes $\approx 3/4$ of the star visible to a distant observer (Beloborodov 2002).

A burst can have tail emission which is produced by the residual heat of the crustal fracturing (Lyubarsky et al. 2002) or bombardment of the stellar surface by the magnetospheric particles (Beloborodov 2009). The tail emission lasts much longer than a burst, and allows us to sample many full rotations. Studying pulse profiles during burst tails may provide insight into the tail emission region. Interestingly, we find clear phase shifts in some post-burst profiles (e.g., bursts 4 and 5, see Figures 2 and 3), which are not caused by rotation (Section 3.2). We conclude that the source of tail emission, e.g., the hot spot produced by the burst, is slightly shifted in longitude relative to the source of persistent emission.

The pulse profiles measured by *XMM-Newton* (Figure 4) also hint at the appearance of a new hot spot. The immediate post-burst pulse profile shows an additional peak at phase ~ 0.3 (Figure 4(b)), which may correspond to the new hot spot. Its emission added to the pulsed persistent source results in a phase shift, which returns to zero as the luminosity of the new hot spot decays and the persistent source dominates again (Figure 2).

4.2. Burst Spectra and Their Evolution

Interesting correlations between burst spectral properties have been seen in some magnetars. For example, Göğüş et al. (2001) reported an anti-correlation between fluence and hardness ratio in the bursts of SGR 1806–20 and SGR 1900+14; however, Gavriil et al. (2004) observed the opposite trend between the same properties in the bursts of 1E 2259+589. While detailed studies of such correlations here are not possible due to the limited number of bursts and small statistics in each burst, we note that there seems to be a hint of a positive correlation between L_{90} and kT (see Table 1).

The source flux returns to the pre-burst value on the kilo-second timescale. Such a short timescale suggests that the crustal heating was not deep, as the large specific heat of the deep crust would hold the energy longer and delay the decay (Kouveliotou et al. 2003). The spectrum of tail emission at ~ 10 –1000 s can be fitted by a blackbody or a power-law model; the blackbody model provides a better fit when the persistent emission is subtracted. The evolution of the blackbody luminosity L_{BB} can be described as a power law with the decay index of 0.8–0.9 (Table 2).¹³ Similar flux decay indices were measured in the 2004 bursts of 1E 1048–5937 (Gavriil et al. 2006, 0.82 ± 0.05) and XTE J1810–197 (Woods et al. 2005, 0.92 ± 0.02). The indices are not far from the crustal cooling model with $L_{\text{BB}} \propto t^{-2/3}$ (Lyubarsky et al. 2002), which was previously used for later time evolution ($t \gtrsim 10,000$ s). The *j*-bundle untwisting (Beloborodov 2009) is usually invoked on even longer timescales, which are associated with the resistive evolution of the magnetosphere.

Note the increase in blackbody area (Figure 5(c)) following a burst. We argue that this is an observational effect rather than a real increase in the physical size. If a burst produced a local hot spot as we argued above, the measured size of the blackbody area would represent the small burst spot at early times, and the large persistent spot later. In order to disentangle the effects of the hot spot and the persistent spot, we also measured the size evolution with the persistent-emission-removed spectrum. The tail was detected significantly above background only for the first ~ 1 ks, and we found that the blackbody area evolved in a similar manner to the trend of the first ~ 1 ks in Figure 5; no clear increase in the size was observed.

In magnetar cooling scenarios, an excited magnetar cools by emitting thermal photons and/or untwisting a *j*-bundle. In both cases, a correlation between flux and hardness is expected (Thompson et al. 2002; Lyutikov 2003; Özel & Güver 2007). Such a correlation has been generally observed in magnetars’ short-term and long-term cooling (e.g., Woods et al. 2005; Gavriil et al. 2006; Scholz et al. 2011; An et al. 2013) with some exceptions (e.g., An et al. 2012; Kaspi et al. 2014). We investigated if such a correlation exists in the tail spectra and found a clear correlation between kT and $\log_{10} L_{\text{BB}}$ (see Figure 5(d)), implying that the burst tails also exhibited a correlation between flux and hardness. Whether the origin of this correlation is the same as for that of the long-term cooling is not clear.

In principle, tail radiation could be the burst “echo” produced by dust scattering around the magnetar (Tiengo et al. 2010). In this scenario, the tail spectrum should soften with time (a result of the scattering cross section being smaller at higher energies); whether or not this is consistent with the observed spectral evolution is unclear. Furthermore, the observed increases in the pulsed flux immediately after the bursts cannot be produced by dust scattering, suggesting that the tail is emitted by the magnetar itself.

4.3. Spectral Feature

We find a spectral feature at ~ 13 keV in the tail emission. Spectral features at a similar energy were previously observed from the burst and tail spectra of several sources, but only with *RXTE* (1E 1048.1–5937, XTE J1810–197, 4U 0142+61;

¹³ The true decay may be somewhat steeper when the persistent emission of 10^{35} erg s^{-1} is subtracted; besides the measured decay index might be affected by undetected low-significance bursts during the tail emission.

Gavriil et al. 2002, 2006, 2011; Woods et al. 2005; Dib et al. 2009). The line energy we found is similar to those previously reported. We note that this is the first detection of the feature with an instrument other than *RXTE*, which demonstrates the effect is not instrumental. We note that the line flux we measured is only $\sim 10\%$ of that previously reported (Gavriil et al. 2002), which could be simply due to the long integration time we used (150 s versus 1 s).

If we interpret the line-like emission as an electron cyclotron feature, the line energy implies that the magnetic field strength is $\sim 10^{12}$ G in the emission region. A magnetic field strength of $\sim 2 \times 10^{15}$ G could be inferred if we interpret the feature due to a proton cyclotron emission, and the line width implies a $\sim 10\%$ change in the magnetic field strength in the emission region. The three detections of the feature from 1E 1048.1–5937 (Gavriil et al. 2002; Dib et al. 2009, and this work) have similar properties (e.g., line energy and width), and probably originated from the same region of the star. If so, it is unlikely that a physical structure can be sustaining at a height of ~ 70 km from the stellar surface (where $B \sim 10^{12}$ G) to power bursts and line features multiple times over a decade. However, a strong multipolar magnetic field (10^{15} G) near the surface in a volume of ~ 1 km³ has enough energy to power multiple bursts and the line feature, suggesting that the line feature could be from proton cyclotron emission. Nevertheless, an interesting question is how different sources which may have different magnetic fields (1E 1048.1–5937, XTE J1810–197, and 4U 0142+61) with different spectral and temporal properties show similar features at such similar energies.

5. CONCLUSIONS

We presented detailed spectral and temporal analyses of eight X-ray bursts from magnetar 1E 1048.1–5937 detected with *NuSTAR*, one of which was simultaneously observed with *XMM-Newton*. The bursts exhibited a fast rise and decay with T_{90} intervals of 1–4 s, and their spectra can be described with single blackbody models having $kT \sim 6$ –8 keV for the T_{90} intervals. All the bursts showed tail emission which can be described with temporally relaxing blackbody models. The flux relaxations of the tail emission followed a power-law decay having decay indices 0.8–0.9. We confirm the existence of an emission feature at ~ 13 keV observed in burst and tail spectra of the source in the past. Finally, we note that similar spectral features at a similar energy have been seen in bursts of several magnetars with different spectral and temporal properties. This requires further theoretical interpretations.

This work was supported under NASA Contract No. NNG08FD60C, and made use of data from the *NuSTAR* mission,

a project led by the California Institute of Technology, managed by the Jet Propulsion Laboratory, and funded by the National Aeronautics and Space Administration. We thank the *NuSTAR* Operations, Software and Calibration teams for support with the execution and analysis of these observations. This research has made use of the *NuSTAR* Data Analysis Software (NuSTAR-DAS) jointly developed by the ASI Science Data Center (ASDC, Italy) and the California Institute of Technology (USA). V.M.K. acknowledges support from an NSERC Discovery Grant, the FQRNT Centre de Recherche Astrophysique du Québec, an R. Howard Webster Foundation Fellowship from the Canadian Institute for Advanced Research (CIFAR), the Canada Research Chairs Program, and the Lorne Trottier Chair in Astrophysics and Cosmology. A.M.B. acknowledges the support by NASA grants NNX10AI72G and NNX13AI34G.

REFERENCES

- An, H., Kaspi, V. K., Archibald, R., & Cumming, A. 2013, *ApJ*, 763, 82
 An, H., Kaspi, V. K., Tomsick, J. A., et al. 2012, *ApJ*, 757, 68
 Beloborodov, A. M. 2002, *ApJL*, 566, L85
 Beloborodov, A. M. 2009, *ApJ*, 703, 1044
 Churazov, E., Gilfanov, M., Forman, W., & Jones, C. 1996, *ApJ*, 471, 673
 Dib, R., Kaspi, V. M., & Gavriil, F. P. 2009, *ApJ*, 702, 614
 Duncan, R. C., & Thompson, C. 1992, *ApJL*, 392, L9
 Durant, M., & van Kerkwijk, M. H. 2006, *ApJ*, 650, 1070
 Feroci, M., Hurley, K., Duncan, R. C., & Thompson, C. 2001, *ApJ*, 549, 1021
 Gavriil, F. P., Dib, R., & Kaspi, V. M. 2011, *ApJ*, 736, 138
 Gavriil, F. P., Kaspi, V. M., & Woods, P. M. 2002, *Natur*, 419, 142
 Gavriil, F. P., Kaspi, V. M., & Woods, P. M. 2004, *ApJ*, 607, 959
 Gavriil, F. P., Kaspi, V. M., & Woods, P. M. 2006, *ApJ*, 641, 418
 Göğüş, E., Kouveliotou, C., Woods, P. M., et al. 2001, *ApJ*, 558, 228
 Göğüş, E., Woods, P. M., Kouveliotou, C., et al. 2011, *ApJ*, 740, 55
 Harrison, F. A., Craig, W. W., Christensen, F. E., et al. 2013, *ApJ*, 770, 103
 Israel, G. L., Romano, P., Mangano, V., et al. 2008, *ApJ*, 685, 1114
 Kaspi, V. M., Archibald, R. F., Bhalerao, V., et al. 2014, *ApJ*, 786, 84
 Kaspi, V. M., Gavriil, F. P., Woods, P. M., et al. 2003, *ApJL*, 588, L93
 Kouveliotou, C., Dieters, S., Strohmayer, T., et al. 1998, *Natur*, 393, 235
 Kouveliotou, C., Eichler, D., Woods, P. M., et al. 2003, *ApJL*, 596, L79
 Lenters, G. T., Woods, P. M., Goupell, J. E., et al. 2003, *ApJ*, 587, 761
 Lin, L., Göğüş, E., Baring, M. G., et al. 2012, *ApJ*, 756, 54
 Lyubarsky, Y., Eichler, D., & Thompson, C. 2002, *ApJL*, 580, L69
 Lyutikov, M. 2003, *MNRAS*, 346, 540
 Olausen, S. A., & Kaspi, V. M. 2014, *ApJS*, 212, 6
 Özel, F., & Güver, T. 2007, *ApJ*, 659, 141
 Scholz, P., & Kaspi, V. M. 2011, *ApJ*, 739, 94
 Tam, C. R., Gavriil, F. P., Dib, R., et al. 2008, *ApJ*, 677, 503
 Thompson, C., & Duncan, R. C. 1995, *MNRAS*, 275, 255
 Thompson, C., & Duncan, R. C. 1996, *ApJ*, 473, 322
 Thompson, C., Lyutikov, M., & Kulkarni, S. R. 2002, *ApJ*, 574, 332
 Tiengo, A., Esposito, P., Mereghetti, S., et al. 2010, *ApJ*, 710, 227
 Tiengo, A., Esposito, P., Mereghetti, S., et al. 2013, *Natur*, 500, 312
 van der Horst, A. J., Kouveliotou, C., Gorgone, N. M., et al. 2012, *ApJ*, 749, 122
 Vasisht, G., & Gotthelf, E. V. 1997, *ApJL*, 486, L129
 Woods, P. M., Kouveliotou, C., Gavriil, F. P., et al. 2005, *ApJ*, 629, 985